

Mapping the mechanical anisotropy of the lithosphere using a 2D wavelet coherence, and its application to Australia

J.F. Kirby*, C.J. Swain

Western Australian Centre for Geodesy, Curtin University of Technology, GPO Box U1987, Perth 6845, Australia

Received 29 July 2005; received in revised form 29 November 2005; accepted 10 March 2006

Abstract

We develop a new method for imaging the spatial variations of the anisotropy of the flexural response of the lithosphere, and apply it to recent topographic and gravity data sets over Australia. The method uses two-dimensional Morlet wavelet transforms, superposed in a strictly controlled geometry, to estimate the auto- and cross-spectra of the two data sets in a number of different directions. The resulting wavelet coherence is a function of scale, or wavelength, as well as orientation, and is inverted, at each spatial location, for the three parameters of an anisotropic, thin elastic plate model, i.e., maximum and minimum flexural rigidities and the orientation of the maximum. Extensive tests of the method on synthetic anisotropic, but uniform, data sets, show that it retrieves the amplitude and orientation of the anisotropy with useful accuracy.

The results for Australia west of 143°E show a strong correlation with the shallower layers (75–175 km) of a recent model of seismic SV wave azimuthal anisotropy. The ‘weak’ axes (i.e., of minimum flexural rigidity) in most cases are approximately at right angles to the fast axes of the seismic anisotropy, implying that, for Precambrian Australia, they arise from the same source. This is most likely deformation resulting from the most recent episode of orogeny.

© 2006 Elsevier B.V. All rights reserved.

PACS: 91.45.Sx

Keywords: Isostasy; Anisotropy; Lithosphere; Wavelets; Australia

1. Introduction

Estimates of the mechanical strength of the continental and oceanic lithosphere may be obtained from spectral isostatic analyses. The concept of isostasy provides a physical model that relates loading on and within the Earth to the compensating buoyancy of a subsurface density distribution, as in Archimedes’ principle. Current isostatic models and plate tectonic theory describe a mechanically strong lithosphere ‘floating’ on an inviscid,

higher density asthenosphere, where long-term loading is supported by flexure of the lithosphere and the corresponding displacement of the asthenosphere. The degree of this flexure is determined by the lithosphere’s flexural rigidity (D), a measure of its mechanical strength, which is more often expressed in terms of an effective elastic thickness (T_e), the two being related by (e.g., Watts, 2001):

$$D = \frac{E T_e^3}{12(1 - \sigma^2)}, \quad (1)$$

where E is the Young’s modulus and σ is Poisson’s ratio. Hence, these terms, D and T_e , are used interchangeably when referring to the same physical process. The mag-

* Corresponding author. Tel.: +61 8 9266 7701;

fax: +61 8 9266 2703.

E-mail address: J.Kirby@curtin.edu.au (J.F. Kirby).

nitude of T_e (D) depends upon many factors, including the temperature, composition and state of stress of the lithosphere, and controls the tectonic evolution of a region, with large-scale T_e variations known to correlate with tectonic province boundaries and seismicity (e.g., Lowry and Smith, 1995).

The lithosphere's thickness can be characterised in several ways. Its thermal thickness, corresponding to the depth at which heat transfer mechanisms change from conduction to convection, can reach magnitudes of up to 350 km (e.g., Artemieva and Mooney, 2001). Its seismogenic thickness, governed by the depth to the brittle/ductile transition, has values reaching 25 km (e.g., Watts and Burov, 2003). The continental elastic thickness, however, is not a physical length parameter, and does not correspond to the depth to which lithospheric rocks behave elastically, as has been suggested in the past (e.g., McNutt, 1990), although there may be some correlation in the oceans (e.g., Watts, 1978). Burov and Diment (1995) and Watts and Burov (2003) have demonstrated that T_e represents the thickness of an equivalent *elastic plate* that best models the flexural properties of the lithosphere, regardless of its actual rheology. As such, T_e is a mechanical, rather than geometrical, property, and indeed, some researchers prefer to present results in terms of the flexural rigidity, which avoids assumptions of the associated elastic constants E and σ .

In the spectral isostatic method, the Bouguer gravity anomaly and topographic signature are compared via the construction of two wavelength-dependent functions, the *admittance* and *coherence*. The former is essentially a transfer function from topography to gravity, while the latter is the square of the correlation coefficient in the wavenumber (spatial frequency) domain between these signals. The reasoning goes that large topographic features (loads) will flex even strong plates: the loads are buoyed by isostatic compensation which generates large Bouguer anomalies, resulting in a coherence that approaches unity. Smaller features, in contrast, will be adequately supported by the plate's mechanical strength, generating little or no associated Bouguer anomaly: the coherence at these wavelengths approaches zero. The *transition wavelength* at which the coherence approximates 0.5 is indicative of the scale at which isostatic compensation begins to prevail over mechanical support, as load size increases. Within a strong/thick plate, the transition wavelength has large values; whereas within weak/thin plates, the coherence "rolls-over" at shorter wavelengths. In the classical method, both admittance and coherence are computed in the Fourier domain (e.g., Forsyth, 1985), though in recent work, their relationship has been analysed through the wavelet transform (Stark

et al., 2003; Kirby and Swain, 2004). By comparing predictions from theoretical loading models with the observed admittance and coherence, T_e may, in principle, be determined.

The theoretical model most commonly used to interpret the observations is the flexure of a *thin* elastic plate (e.g., Watts, 2001). Such a plate has the properties that its vertical deflections under loading are small compared to its thickness, and that this thickness is small compared to the lateral extent of the plate, which is true in a majority of tectonic regimes. An alternative model is that of the thick plate (Comer, 1983; Wolf, 1985). However, Banks et al. (1977) and Watts (2001) conclude that the errors that arise through the approximations and assumptions of thin-plate theory are not important, considering that most of these errors are manifest in the short wavelengths, and not around the transition wavelengths of importance in T_e -estimation. Hence, thin plate theory is adequate at modelling most tectonic environments.

In the past, theoretical admittances and coherences have been computed from the loading of an *isotropic* and *uniform* thin elastic plate, that is, one in which the loading response is equal in all directions from the applied load. However, given the highly variable temperature, compositional and stress regimes present in the lithosphere, and the existence of faulting of all orientations, it is clear that the loading response of the lithosphere will not generally be isotropic or uniform at all scales.

More recently, several researchers have attempted to detect anisotropy in the flexural rigidity by analysing observed data with two-dimensional (2D) techniques (such as maximum entropy or multitaper spectral estimators) and interpreting the results as evidence of anisotropy (e.g., Lowry and Smith, 1995; Simons et al., 2000, 2003; Audet and Mareschal, 2004). These studies, however, have not used an anisotropic plate model by which to interpret their observed coherences.

Using such a plate model, anisotropic estimates of T_e were computed for central Australia by Swain and Kirby (2003b). In this approach, an observed 2D coherence, computed by the multitaper method, was compared with a theoretical coherence predicted by loading on an anisotropic, thin elastic plate with assumed values of T_x , T_y (being the anisotropic elastic thicknesses) and the orientation of weakest rigidity, and based on a straightforward modification of the isotropic equations of Banks et al. (2001). The estimated values of T_x , T_y and anisotropy direction for central Australia were those that minimised the misfit between theoretical and observed coherence.

The present study forms an extension to this work. Differences with Swain and Kirby (2003b) involve the replacement of the multitaper Fourier method by the

wavelet transform through which to estimate observed coherence (Kirby and Swain, 2004), and an anisotropic development of coherence estimation. Swain and Kirby (2006) have also extended the “predicted coherence method” of Forsyth (1985) to the wavelet domain for isotropic T_e -estimation, and while we have also tackled anisotropic T_e -estimation in this fashion, the following study concerns the approach using theoretical coherence equations with an assumed ratio of subsurface to surface loads. This assumption means that our anisotropy directions (but not magnitudes) will be strictly comparable with those measured directly from coherence anisotropy, as in the studies by Simons et al. (2003), for example, which do not depend on the thin plate model. As noted below, the differences between the results of these two approaches are generally quite small, though occasionally significant, and in particular, the conclusions of the present study are not changed by the use of Forsyth’s method.

2. The wavelet admittance and coherence

2.1. Isotropic case

In the classical method of spectral isostatic analysis, the Fourier transform is utilised to estimate the frequency characteristics of the isostatic admittance and coherence, whether through the conventional periodogram, or more recently multitaper methods. The drawback of the isotropic Fourier approach is that only one estimate of the coherence (and admittance) is achievable for a data window. These parameters are dependent on wavenumber only, and all spatial information is irretrievable. The most common method used to circumvent this deficiency involved the windowed Fourier transform (WFT) (e.g., Lowry and Smith, 1994; Poudjom Djomani et al., 1999; Pérez-Gussinyé et al., 2004). In this approach, the coherence and admittance are estimated within a moving window, smaller than the study area, as in the Gabor transform. Within each window, comparison of the observed and theoretical coherences yields T_e values that can be mapped, giving the variation of elastic thickness over the study area. The choice of window size depends upon the strength of the plate being mapped, with larger windows needed to estimate larger plate thicknesses, due to their larger transition wavelengths (e.g., Macario et al., 1995).

However, the WFT suffers from two shortcomings. First, owing to its fixed window size, it performs best on data having a narrow wavenumber bandwidth, and cannot easily resolve broadband signals (e.g., Addison, 2002). Even though gravity and topography data have

red spectra, they are not narrow-band signals. The second disadvantage lies in the trade-off between window size and resolution. On the one hand, use of a small window can better represent the spatial variation of T_e over a large study area, though it will not resolve any transition wavelengths longer than the window size. On the other hand, while larger windows can resolve longer wavelengths, they run the risk of averaging the elastic thicknesses within a region of highly variable T_e , thus not representing the high-frequency variations on the overall map.

The wavelet transform was developed by Grossman and Morlet (1984) to overcome the deficiencies of the WFT. Whereas Fourier coefficients are dependent on wavenumber only, wavelet coefficients are functions of both wavenumber and spatial coordinates. This valuable extra information is achieved through convolution of a signal with localised basis functions (the wavelet), rather than with the infinitely extending (though in practice truncated) sinusoids of Fourier analysis.

In this study, we use the 2D continuous wavelet transform (CWT) in place of the Fourier transform when computing the auto- and cross-correlations of gravity and topography data needed in admittance and coherence analyses. This then gives these quantities as functions of wavenumber, geographical location, and azimuth, so that a map of the directional variations of flexural rigidity may be computed. Kirby (2005) provides a brief introduction to the 2D CWT, while a more complete discussion can be found in, e.g., Farge (1992) or Antoine et al. (2004).

In practice, the 2D CWT of a signal is computed via the Fourier transform, which speeds up the convolution procedure. For a 2D space-domain signal $y(\mathbf{x})$, its wavelet coefficients, $\tilde{y}(s, \mathbf{x}, \theta)$, are generated through a computational implementation of the following formula:

$$\tilde{y}(s, \mathbf{x}, \theta) = \mathbf{F}^{-1} \{ \hat{y}(\mathbf{k}) \hat{\psi}_{s,\theta}^*(\mathbf{k}) \}, \quad (2)$$

where $\mathbf{x} = (x, y)$ is the space-domain position vector, for grid eastings (or longitude), x , and grid northings (or latitude), y ; s is the wavelet scale, described later; θ is the rotation parameter, determining the resolving azimuth of the wavelet; $\mathbf{k} = (u, v)$ is the 2D wavenumber, where u is the wavenumber in the x -direction, and v that in the y -direction; \mathbf{F}^{-1} is the inverse 2D Fourier transform; $\hat{y}(\mathbf{k})$ is the 2D Fourier transform of the signal.

The $\hat{\psi}_{s,\theta}^*(\mathbf{k})$ are the complex conjugates of the 2D Fourier transforms of the ‘daughter’ wavelets. They are derived from a ‘mother’ wavelet, $\hat{\psi}(\mathbf{k})$, through the relationship:

$$\hat{\psi}_{s,\theta}(\mathbf{k}) = s \hat{\psi}(s\Omega(\theta)\mathbf{k}). \quad (3)$$

That is, the mother wavelet is both dilated and weighted by the chosen scale, s , and also rotated through a chosen angle θ , to yield a daughter wavelet. In Eq. (3), the rotation matrix, $\Omega(\theta)$, for positive-anticlockwise rotations, θ , of the mother wavelet is given by

$$\Omega(\theta) = \begin{pmatrix} \cos \theta & \sin \theta \\ -\sin \theta & \cos \theta \end{pmatrix}. \quad (4)$$

The translation of the daughter wavelet over the signal is achieved by convolution in the space-domain, or equivalently via Eq. (2) in the wavenumber-domain, enabling a region-by-region analysis of the signal. The computation is performed for many values of scale and azimuth, where the former are usually chosen to span the complete bandwidth of the signal, and our choice of the latter is discussed in Sections 2.2, 5 and 6. The wavelet scale, s , determines the width (dilation) of the daughter wavelet in the space domain, and hence determines resolution. At large scales, the wavelet coefficients reveal long wavelengths in the data; at small scales they show short wavelengths. In this regard, the wavelet transform resembles a series of band-pass filters. It is the combination of this dilation with the translation which allows the frequency characteristics at each location of the signal to be revealed.

The choice of analysing wavelet is important with regards to a final interpretation of the CWT, particularly when computing the isostatic coherence. First, the Fourier transform of some real-valued, asymmetrically distributed data, $y(\mathbf{x})$, is a Hermitian function, $\hat{y}(\mathbf{k})$, whose real component is an even function, and imaginary component is an odd function. The imaginary part, $\text{Im}[\hat{y}(\mathbf{k})]$, is shown schematically in Fig. 1, and it can be seen that the lower two quadrants in the wavenumber domain contain redundant information: they are merely (negative) mirrors of the upper two quadrants for the imaginary component, and positive mirrors for the real component (not shown). Hence, if isotropic information from a signal is desired, then only the upper two quadrants need be analysed.

Now consider the isostatic coherence. Conventionally, the Fourier coherence between Bouguer gravity anomalies, $b(\mathbf{x})$, and topography/bathymetry, $h(\mathbf{x})$, is computed in the wavenumber domain from averages of their auto- and cross-spectra (Forsyth, 1985):

$$\gamma_F^2(|\mathbf{k}|) = \frac{|\langle \hat{b} \hat{h}^* \rangle_{|\mathbf{k}|}|^2}{\langle \hat{b} \hat{b}^* \rangle_{|\mathbf{k}|} \langle \hat{h} \hat{h}^* \rangle_{|\mathbf{k}|}}, \quad (5)$$

where the $\langle \cdot \rangle_{|\mathbf{k}|}$ represents an averaging over annuli of similar scalar wavenumber. Alternatively, other methods of averaging may be performed, such as through one of

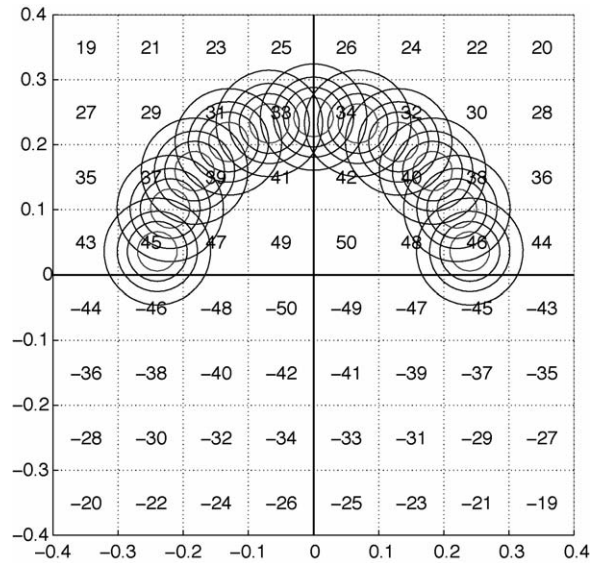


Fig. 1. The imaginary part of the Fourier transform of some real-valued data, showing the eleven constituent Morlet wavelets that comprise an isotropic fan wavelet geometry of azimuthal extent $\Delta\theta = 180^\circ$. Axes are u and v wavenumber in rad/km.

the multitaper spectral estimators (e.g., Simons et al., 2000, 2003), in which case the Fourier coherence is a function of 2D, and not 1D, wavenumber. What is important, though, is that some form of averaging must be performed: if not then the numerator and denominator in Eq. (5) cancel and the coherence is unity at all wavenumbers.

With the wavelet coherence, we perform an azimuthal averaging in the wavenumber domain, constrained by the geometry of the ‘fan’ wavelet (Kirby, 2005). The fan wavelet is constructed from a strictly controlled superposition of 2D Morlet wavelets which are able to exactly reproduce the Fourier power spectrum of a signal (Kirby, 2005), without further computation (e.g., Stark et al., 2003).

The procedure to compute the wavelet coherence involves, first, taking the Morlet wavelet transform, at some starting azimuth, θ , of the Bouguer anomaly [cf. Eq. (2)]:

$$\tilde{b}_{s\theta} \equiv \tilde{b}^M(s, \mathbf{x}, \theta) = \mathbf{F}^{-1} \{ \hat{b}(\mathbf{k}) \hat{\psi}_{s,\theta}^{M*}(\mathbf{k}) \}, \quad (6)$$

where the first term indicates the convenient short-hand notation used hereafter for the Morlet wavelet coefficients. The Fourier transform of the 2D Morlet (daughter) wavelet, at some scale s and azimuth θ , is

$$\hat{\psi}_{s,\theta}^M(\mathbf{k}) = s e^{-[(su - |\mathbf{k}_0| \cos \theta)^2 + (sv - |\mathbf{k}_0| \sin \theta)^2]/2}, \quad (7)$$

where $|\mathbf{k}_0| = \pi\sqrt{2/\ln 2} \approx 5.336$ (e.g., Farge, 1992). The $\tilde{b}_{s\theta}$ are then computed at a number of other az-

imuths, determined according to the fan wavelet geometry in the following manner. If a total azimuthal extent of $\Delta\theta$ is required, then the necessary number of Morlet wavelet transforms is given by $N_\theta = \text{int}(\Delta\theta/\delta\theta)$, where $\delta\theta$ is the azimuthal increment between successive Morlet wavelet transforms. It was determined that, in order to avoid azimuthal over- and under-sampling, the azimuthal increment should have a value of $\delta\theta = 2\sqrt{\ln(4/3)} \ln 2/\pi \approx 16.3^\circ$ (Kirby, 2005). This procedure is illustrated schematically in Fig. 1, for $\Delta\theta = 180^\circ$, giving $N_\theta = 11$. Each set of concentric circles represents a single Morlet wavelet, and N_θ sets of gravity wavelet coefficients, $\tilde{b}_{sx\theta}$, are obtained by multiplying each Morlet wavelet by the gravity Fourier transform, according to Eq. (6). [Incidentally, averaging all 11 Morlet wavelets yields the fan wavelet shown in Fig. 1 of Kirby and Swain (2004).] The procedure is also performed at the same azimuths on the topography, yielding N_θ sets of topography wavelet coefficients, $\tilde{h}_{sx\theta}$.

In order to compute the wavelet coherence, the auto- and cross-spectra of the gravity and topography wavelet coefficients are averaged over the N_θ azimuths, rather than averaging the wavelet coefficients themselves, e.g.:

$$\langle \tilde{b}_{sx\theta} \tilde{h}_{sx\theta}^* \rangle_\theta \equiv \frac{1}{N_\theta} \sum_{n=1}^{N_\theta} \{ \tilde{b}_{sx\theta} \tilde{h}_{sx\theta}^* \}_n \quad (8)$$

for $\theta_n : n = [1, N_\theta]$, with Eq. (8) defining the notation used following. Then, by analogy with Eq. (5), the wavelet coherence over an azimuthal extent $\Delta\theta$ is computed from:

$$\gamma_{\text{W}}^2(s, \mathbf{x}, \theta) = \frac{|\langle \tilde{b}_{sx\theta} \tilde{h}_{sx\theta}^* \rangle_\theta|^2}{\langle \tilde{b}_{sx\theta} \tilde{b}_{sx\theta}^* \rangle_\theta \langle \tilde{h}_{sx\theta} \tilde{h}_{sx\theta}^* \rangle_\theta}. \quad (9)$$

As can be seen, the geometry in Fig. 1 is isotropic as the 11 Morlet wavelets capture all of the data in the upper two quadrants, although there is some unavoidable leakage into the lower two quadrants. Hence, if $\Delta\theta = 180^\circ$, then the wavelet coherence in Eq. (9) is isotropic and θ -independent: $\gamma_{\text{W}}^2(s, \mathbf{x})$. This quantity has been shown to be directly comparable with both theoretical and Fourier-derived coherence estimates (Kirby and Swain, 2004). However, if more than 11 Morlet wavelets were used in the superposition, cancellations of the imaginary component of the product $\hat{b}(\mathbf{k}) \hat{\psi}_{s,\theta}^{M*}(\mathbf{k})$ in Eq. (6) would begin to occur in the averaging procedure, owing to the negative reflection of $\text{Im}[\hat{b}(\mathbf{k})]$ about the axis $v = 0$, leading to loss of information. In the extreme case of a ring-shaped geometry ($\Delta\theta \rightarrow 360^\circ$), the cancellations would be total, the wavelet coefficients would have no imaginary components (Kirby, 2005), and the wavelet coherence would be unity.

To enable direct comparison with 1D coherence estimates from the conventional annular-averaging method, Eq. (5), the wavelet method can also yield a global 1D profile, through a complete averaging of the auto- and cross-spectra over the space variable at each scale. Using the notation:

$$\langle \cdot \rangle_{\mathbf{x}} \equiv \frac{1}{N_x N_y} \sum_{i=1}^{N_y} \sum_{j=1}^{N_x} \{ \cdot \}, \quad (10)$$

where the data grids are of size $N_x \times N_y$, the global wavelet coherence is computed by

$$\overline{\gamma}_{\text{W}}^2(s, \theta) = \frac{\langle \langle \tilde{b}_{sx\theta} \tilde{h}_{sx\theta}^* \rangle_\theta \rangle_{\mathbf{x}} \langle \langle \tilde{b}_{sx\theta} \tilde{h}_{sx\theta}^* \rangle_\theta \rangle_{\mathbf{x}}}{\langle \langle \tilde{b}_{sx\theta} \tilde{b}_{sx\theta}^* \rangle_\theta \rangle_{\mathbf{x}} \langle \langle \tilde{h}_{sx\theta} \tilde{h}_{sx\theta}^* \rangle_\theta \rangle_{\mathbf{x}}}, \quad (11)$$

which is now a function of scale and azimuth only.

Finally, the scale of each daughter wavelet must be related to an ‘equivalent Fourier wavenumber’, κ , by taking the wavenumber at which the daughter wavelet has its maximum value (for that scale) to be representative of the harmonics resolved by that daughter wavelet (e.g., Kirby, 2005). The equivalent Fourier wavenumber for the Morlet wavelet at each scale is given by (Kirby, 2005):

$$\kappa = \frac{|\mathbf{k}_0|}{s}. \quad (12)$$

This enables direct comparison with both theoretical models and estimates from Fourier transform methods. Thus, we now write $\gamma_{\text{W}}^2(\kappa, \mathbf{x}, \theta)$ for the wavelet coherence, and $\overline{\gamma}_{\text{W}}^2(\kappa, \theta)$ for the global wavelet coherence.

2.2. Anisotropic case

As pointed out by Kirby and Swain (2004), the case of anisotropic T_e can be studied by limiting the azimuthal extent $\Delta\theta$. If $2\delta\theta < \Delta\theta < 180^\circ$, then the averaged auto- and cross-spectra [Eq. (8)] become directional. However, the coherence formulae, Eqs. (9) and (11), require averaging over at least two azimuths, since if only one azimuth transform is computed, the numerator and denominator are equal, and the coherence is always unity.

Anisotropy in the wavelet coherence can be revealed by computation at a number of central (or resolving) azimuths, Θ , spanning the range $0^\circ \leq \Theta < 180^\circ$, to ensure good directional sampling. In this study we chose six central azimuths from $\Theta = 0^\circ$ to 150° in increments of $\delta\Theta = 30^\circ$, each averaging $N_\theta = 5$ auto- and cross-spectra over $\Delta\theta = 90^\circ$, although other values of $\Delta\theta$ and $\delta\Theta$ were tested (Section 5). Thus, the spectra were computed from $\theta = -45^\circ$ to $+45^\circ$, giving $\gamma_{\text{W}}^2(\kappa, \mathbf{x}, \Theta)$ at $\Theta = 0^\circ$; then from $\theta = -15^\circ$ to $+75^\circ$, giving γ_{W}^2 at

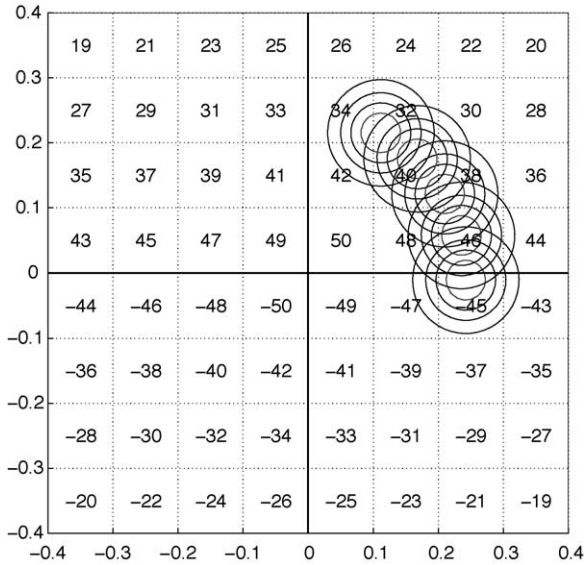


Fig. 2. The imaginary part of the Fourier transform of some real-valued data, showing the five constituent Morlet wavelets that comprise an anisotropic fan wavelet geometry of central azimuth $\Theta = 30^\circ$ and azimuthal extent $\Delta\theta = 90^\circ$. Axes are u and v wavenumber in rad/km.

$\Theta = 30^\circ$, etc. Fig. 2 shows the wavelet geometry used for the anisotropic azimuthal averaging of the auto- and cross-spectra at a central azimuth $\Theta = 30^\circ$.

Therefore, at each geographic location of the study area, \mathbf{x}_0 , we now have six anisotropic estimates of the wavelet coherence, $\gamma_{\mathbb{W}}^2(\kappa, \mathbf{x}_0, \Theta)$.

3. The anisotropic plate model

3.1. An orthotropic plate

Conventional thin plate modelling assumes a lithosphere parameterised by a single flexural rigidity, D . That is, the response of the plate to loading is assumed to be isotropic. In the present study, and in Swain and Kirby (2003b), we model the observed coherences with an orthotropic plate. As described in Timoshenko and Woinowsky-Krieger (1959), an orthotropic plate is one whose elastic properties have at least two orthogonal planes of symmetry, and where the anisotropy may be parameterised by two orthogonal rigidities, D_x and D_y , being the plate strengths in these directions. However, as discussed in the Introduction, isostatic studies typically have results presented in terms of the elastic thickness rather than flexural rigidity. So even though it is rather counter-intuitive to speak of a “thickness in the x -direction” for example, we follow convention, and relate the anisotropic rigidities to their elastic thickness

counterparts through analogy with Eq. (1):

$$D_x = \frac{E T_x^3}{12(1 - \sigma^2)}, \quad (13)$$

and similarly for D_y , where in this study we have assumed uniform and isotropic values of $E = 100$ GPa, and $\sigma = 0.25$. In reality, these ‘constants’ could vary geographically, and Chevrot and van der Hilst (2000) determined a range of 0.23–0.28 for Poisson’s ratio in Australia. Nevertheless, since lateral variations in these quantities should affect the coherence at a point equally in all directions, we assume uniformity. These constants could also vary directionally, and while orthotropic plate theory can account for quantities like E_x and σ_y , in the absence of such information for Australia, we assume isotropy in these constants.

In general, for an initial load $\ell(\mathbf{x})$, the vertical deflection, $w(\mathbf{x})$, experienced by a uniform, orthotropic, thin elastic plate overlying an inviscid fluid of density ρ_m is given by (e.g., Timoshenko and Woinowsky-Krieger, 1959):

$$D_x \frac{\partial^4 w(\mathbf{x})}{\partial x^4} + 2H \frac{\partial^4 w(\mathbf{x})}{\partial x^2 \partial y^2} + D_y \frac{\partial^4 w(\mathbf{x})}{\partial y^4} + \rho_m g w(\mathbf{x}) = \ell(\mathbf{x}), \quad (14)$$

where the last term on the left-hand side is the buoyancy force arising from displacement of the underlying fluid, and g is the gravity acceleration. Following Timoshenko and Woinowsky-Krieger (1959) and Swain and Kirby (2003b), we can approximate H by

$$H \approx \sqrt{D_x D_y}. \quad (15)$$

In general, the orthotropic plate equation [Eq. (14)] can be solved by a finite difference method, using sparse matrix techniques (e.g., Kirby and Swain, 2004). For uniform D_x , D_y , and ρ_m , Eq. (14) is far more easily solved via the Fourier transform:

$$[(\sqrt{D_x} u^2 + \sqrt{D_y} v^2)^2 + \rho_m g] \hat{w}(\mathbf{k}) = \hat{\ell}(\mathbf{k}), \quad (16)$$

using the approximation, Eq. (15). Recall $\mathbf{k} = (u, v)$. Solution of Eq. (16), through either of the two methods presented in Sections 3.3 and 3.4, yields the ‘observed’ Bouguer anomaly and topography for the model, and also the theoretical coherence and admittance.

To account for different directions of anisotropy, the u and v axes can be rotated through an angle β , the direction of anisotropy, defined as the (positive anticlockwise) angle from the positive u axis to the positive u' axis [cf.

Eq. (4)]:

$$\begin{pmatrix} u' \\ v' \end{pmatrix} = \begin{pmatrix} \cos \beta & \sin \beta \\ -\sin \beta & \cos \beta \end{pmatrix} \begin{pmatrix} u \\ v \end{pmatrix}. \quad (17)$$

For use in the following discussions, and from Eq. (16), we define a ‘flexural operator’ in the rotated frame:

$$\Lambda(\mathbf{k}) \equiv (\sqrt{D_x} u'^2 + \sqrt{D_y} v'^2)^2. \quad (18)$$

Note that when $D_x = D_y = D$, $\Lambda(\mathbf{k}) \rightarrow D|\mathbf{k}|^4$, and Eq. (16) reduces to the conventional isotropic plate model.

3.2. Random fractal loads

Following Macario et al. (1995) [and further discussed in Swain and Kirby (2003a,b)], initial synthetic surface and subsurface loads are emplaced on and within a thin elastic plate, and the resulting synthetic topography and Bouguer anomaly are determined from solutions to the thin plate differential equation. We tested two such plate models: those of Banks et al. (2001) and Forsyth (1985).

We created two random fractal surfaces, $s_T(\mathbf{x})$ and $s_B(\mathbf{x})$, using the 2D spectral synthesis algorithm of Peitgen and Saupe (1988). We chose the fractal dimension of both surfaces to be 2.5. These surfaces then had their mean subtracted, and were standardised to unit variance. An example of such a surface is shown in Fig. 3. Each surface was then multiplied by 100 m, hence representing the amplitude of some load. The correlation coefficient between the surfaces [R in Macario et al., 1995] was set to zero, to make the loads uncorrelated as required for the coherence to be diagnostic of the elastic thickness (Forsyth, 1985).

3.3. The plate model of Banks et al.

The formulation of Banks et al. (2001) in the continental case requires two loads: an initial surface load due to the topography, and an initial subsurface load representing the variable density of a thin layer. This thin layer is emplaced at depth z_1 within the crust, though they also consider the gravity effect of the density contrast, $\Delta\rho$, at the Moho. Hence, in Eq. (14) we set $\ell(\mathbf{x}) = -\ell_T(\mathbf{x}) - \ell_B(\mathbf{x})$, where the loads are derived from the fractal surfaces as: $\ell_T(\mathbf{x}) = \rho_c g s_T(\mathbf{x})$ and $\ell_B(\mathbf{x}) = f\rho_c g s_B(\mathbf{x})$. The mean crustal density is ρ_c , and f is the subsurface-to-surface loading ratio, which we set to a constant value [though see Swain and Kirby (2003a) for a discussion concerning the effect on f of different fractal dimensions for the two loads].

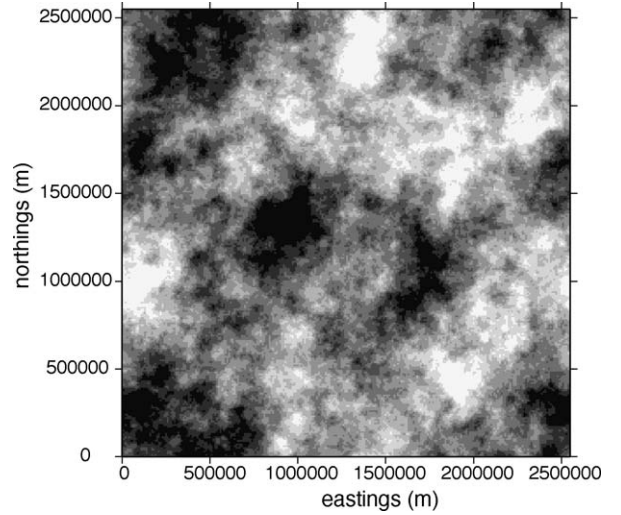


Fig. 3. One of the random fractal surfaces (fractal dimension 2.5) used as input to form an initial load on the orthotropic plate. Grey scale ± 3.5 (dimensionless).

To determine the ‘observed’ Bouguer anomaly and topography from the model, a value for each of T_x , T_y and β is assumed. Eq. (13) then determines the anisotropic flexural rigidities. Rearranging the flexural equation, Eq. (16), gives the (Fourier transform of) the plate deflection as

$$\hat{w}(\mathbf{k}) = \frac{-\hat{\ell}_T(\mathbf{k}) - \hat{\ell}_B(\mathbf{k})}{\Lambda(\mathbf{k}) + \rho_m g}, \quad (19)$$

which is the anisotropic version of Eq. (16) in Banks et al. (2001). Following Banks et al. (2001), it is a simple matter to generalise their Eqs. (17) and (18) to the anisotropic case. The resulting surface topography after loading is the sum of the initial surface load amplitude and the resulting plate deflection:

$$\hat{h}(\mathbf{k}) = \frac{\hat{\ell}_T(\mathbf{k})}{\rho_c g} + \hat{w}(\mathbf{k}), \quad (20)$$

while the surface Bouguer anomaly is estimated from the upward continued thin layer and Moho deflections:

$$\hat{b}(\mathbf{k}) = 2\pi G \left(\frac{e^{-|\mathbf{k}|z_1} \hat{\ell}_B(\mathbf{k})}{g} + \Delta\rho e^{-|\mathbf{k}|z_m} \hat{w}(\mathbf{k}) \right), \quad (21)$$

where $\Delta\rho = \rho_m - \rho_c$. Inverse Fourier transformation of Eqs. (20) and (21) then gives $h(\mathbf{x})$ and $b(\mathbf{x})$.

3.4. Forsyth’s plate model

In the approach of Forsyth (1985), the two loads are an initial topography: $h_1(\mathbf{x}) = s_T(\mathbf{x})$; the relief on the Moho: $w_1(\mathbf{x}) = f\rho_c s_B(\mathbf{x})/\Delta\rho$. If values of T_x , T_y and β

are assumed, the ‘observed’ topography and Bouguer anomaly after flexure can be determined. Again, the isotropic equations are readily converted to anisotropic ones, using Eq. (18). Forsyth’s equations for ξ and ϕ become:

$$\xi(\mathbf{k}) = 1 + \frac{\Lambda(\mathbf{k})}{\Delta\rho g}, \quad \phi(\mathbf{k}) = 1 + \frac{\Lambda(\mathbf{k})}{\rho_c g}, \quad (22)$$

and the final surface topography and Moho relief are determined from:

$$\hat{h}(\mathbf{k}) = \hat{h}_I(\mathbf{k}) \left[\frac{\Delta\rho \xi(\mathbf{k})}{\rho_c + \Delta\rho \xi(\mathbf{k})} \right] - \hat{w}_I(\mathbf{k}) \left[\frac{\Delta\rho}{\Delta\rho + \rho_c \phi(\mathbf{k})} \right], \quad (23)$$

and

$$\hat{w}(\mathbf{k}) = -\hat{h}_I(\mathbf{k}) \left[\frac{\rho_c}{\rho_c + \Delta\rho \xi(\mathbf{k})} \right] + \hat{w}_I(\mathbf{k}) \left[\frac{\rho_c \phi(\mathbf{k})}{\Delta\rho + \rho_c \phi(\mathbf{k})} \right], \quad (24)$$

respectively [cf. Forsyth’s Eq. (18)]. An ‘observed’ Bouguer anomaly at the surface may then be estimated from the upward continued Moho relief:

$$\hat{b}(\mathbf{k}) = 2\pi\Delta\rho G e^{-|\mathbf{k}|z_m} \hat{w}(\mathbf{k}), \quad (25)$$

being the anisotropic version of Forsyth’s Eq. (13). Inverse Fourier transformation of Eqs. (23) and (25) then gives $h(\mathbf{x})$ and $b(\mathbf{x})$.

4. Estimation of anisotropic parameters

In the Forsyth (1985) method, a value for T_e is assumed and the isotropic versions of our Eqs. (23) and (24) are solved simultaneously in order to estimate the initial loads from the observed topography and Bouguer gravity, and hence calculate a “predicted coherence”. T_e is then estimated as the value that minimises the misfit between observed and predicted coherence. This method has the advantage that it makes no assumptions about the loading, with f essentially being determined at each wavenumber from the WFT of the data. Swain and Kirby (2003b) showed how to modify this method to estimate T_x , T_y and β for a uniform orthotropic plate model.

In the present study we used a simpler procedure, similar to that used in Kirby and Swain (2004), and inverted the coherence for the three plate parameters using the theoretical formula for coherence (given in the Appendix). This requires the knowledge (or assumption) of the loading ratio and we simply assumed that f is uniform (spatially invariant), isotropic, and wavenumber-independent: we call this the “uniform f ” method. On

this assumption, its variations should affect T_x and T_y equally. When inverting the coherence at each geographic location, we also assumed that the local wavelet spectra are independent, or “decoupled” from adjacent spectra (Stark et al., 2003). The validity of this assumption can be tested by means of non-uniform synthetic models, which we have not used in this study, though Swain and Kirby (2006) present one such (isotropic) model finding that the decoupling assumption is quite reasonable in that case.

It is worth mentioning here that we also tried a wavelet version of Forsyth’s method, in order to test the assumption of uniform, isotropic f . This involved extending our (isotropic) wavelet development of Forsyth (1985)’s approach (Swain and Kirby, 2006) to the case of anisotropy, which has the advantage of also allowing for the possibility of anisotropy in f . The relevant equations are identical to Forsyth’s, with the Fourier transforms of gravity and topography replaced by their wavelet transforms, $D|\mathbf{k}|^4$ replaced by $\Lambda(\mathbf{k})$, and the averaging performed over wavelet azimuth rather than scalar wavenumber. When applied to the synthetic models (see Section 5), the directions of T_e anisotropy given by this method and the uniform f method agree to within $<10^\circ$, which is comparable with the standard deviation of the orientations of axes given in Section 5. The largest differences occur where the T_e anisotropy estimates, with either method, are small. We also used the anisotropic wavelet Forsyth method with the Australian data, obtaining a comparable agreement with the uniform f method, except for part of central Australia, where Forsyth’s method yields larger magnitudes of anisotropy, presumably because of anisotropic (east–west) loading. Because of this agreement we consider that the assumptions about loading made by the uniform f method are justified, at least for Australia and the synthetic models. The results in the rest of this paper are for the uniform f method.

In order to estimate the values of T_x , T_y and β for our orthotropic model at a particular \mathbf{x}_0 , we compare the observed wavelet coherence at all values of Θ with the theoretical coherences of an anisotropic plate in these directions. To calculate such a coherence, we rewrite the flexural operator in polar coordinates in the \mathbf{k} -frame:

$$\Lambda(|\mathbf{k}|, \Theta) = \left[\sqrt{D_x} |\mathbf{k}|^2 \cos^2(\Theta - \beta) + \sqrt{D_y} |\mathbf{k}|^2 \sin^2(\Theta - \beta) \right]^2. \quad (26)$$

The general forms of the theoretical coherences from both Banks and Forsyth models are shown in Appendix A: to compute a theoretical coherence profile, $\gamma_c^2(|\mathbf{k}|, \Theta)$,

in direction Θ from Eqs. (A.1) and (A.5), replace $\Lambda(\mathbf{k})$ with $\Lambda(|\mathbf{k}|, \Theta)$.

Starting with initial estimates of $[T_x, T_y, \beta]$, the differences at all values of Θ between the theoretical coherences, $\gamma_t^2(|\mathbf{k}|, \Theta)$, and observed wavelet coherences, $\gamma_w^2(\kappa, \mathbf{x}_0, \Theta)$, are minimised simultaneously using an iterative damped least squares algorithm similar to the one described in Swain and Kirby (2003b), except that here we assume that the uncertainty of an observed coherence estimate is proportional to $|\mathbf{k}|$, and weight the data as $1/|\mathbf{k}|$. After a number of iterations, stable values for the estimates $[T_x, T_y, \beta]$ are reached. This procedure is then repeated for each geographical location, \mathbf{x}_0 , in the study area, giving estimates in each grid cell. In a very few instances with real data we have found it necessary to use two different starting models, with β differing by 90° , in order to find the global minimum.

Single estimates of $[\bar{T}_x, \bar{T}_y, \bar{\beta}]$ for the whole study area can also be derived by inverting the global wavelet coherence, $\bar{\gamma}_w^2(\kappa, \Theta)$, using the same method.

5. Results for the synthetic models

In this study we only consider *uniform*, anisotropic models, because in such cases the plate equation [Eq. (14)] can be easily and quickly solved using the FFT, as shown above. We generated 100 pairs of random, synthetic Bouguer anomaly and topography grids using the Forsyth plate model, all with $[T_x, T_y, \beta] = [80, 40, 40^\circ]$ and $f = 1$. Then, as discussed in Section 2.2, the anisotropic wavelet coherence from each pair was computed at six central azimuths from $\Theta = 0^\circ$ to 150° , in increments of $\delta\Theta = 30^\circ$, each using $\Delta\theta = 90^\circ$. In order to minimise array sizes and computation time, and to make plots less cluttered, the wavelet auto- and cross-spectra were ‘binned’ into larger grid cells of size $320 \text{ km} \times 320 \text{ km}$, prior to using Eq. (9). It must be stressed that this spatial averaging is performed only for computational convenience, and is not essential: while it has the effect of damping the noise in the coherence at high wavenumbers, it does not significantly alter the estimated values of the transition wavelength, and hence of T_x or T_y . Furthermore, to eliminate edge effects from the Fourier transform, the outer 5% at each side was discarded before implementation of Eq. (11).

Inverting the global wavelet coherence, Eq. (11), for all 100 pairs (using the Forsyth theoretical coherence formula, Eq. (A.5), and assuming $f = 1$), gave $\bar{T}_x = 71 \pm 9 \text{ km}$, $\bar{T}_y = 45 \pm 6 \text{ km}$, and $\bar{\beta} = 39 \pm 10^\circ$ (arithmetic mean \pm standard deviation). The global coherences at the selected Θ values, for one model (#34), are

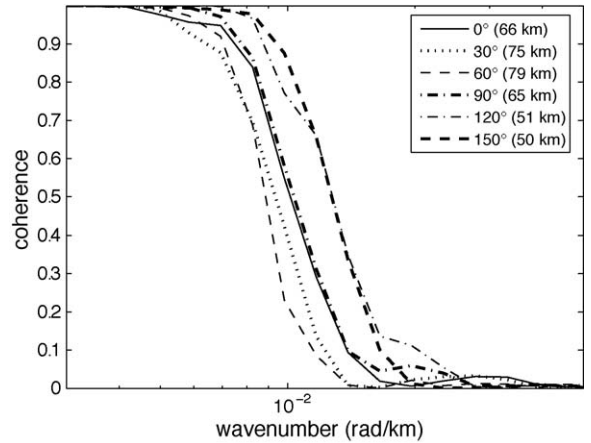


Fig. 4. The global wavelet coherences computed at six indicated central azimuths (Θ), from a Forsyth-style synthetic plate model (#34) with $T_x = 80 \text{ km}$, $T_y = 40 \text{ km}$ and $\beta = 40^\circ$, with $f = 1$. The values in parentheses after Θ are estimated T_e values for that azimuth after inversion of the individual coherence profiles, assuming $f = 1$.

shown in Fig. 4. This particular model gave estimates: $\bar{T}_x = 79.6 \text{ km}$, $\bar{T}_y = 47.6 \text{ km}$, and $\bar{\beta} = 45.0^\circ$. The legend indicates the Θ value for each profile, together with an estimated elastic thickness value at each azimuth (by inversion of the observed global wavelet coherence curves). Clearly though, the anisotropy of the model is being revealed.

Fig. 5 shows the spatial variation in anisotropy for model #34. The ellipses are “ T_e -ellipses”: the length of the major and minor axes indicate the relative magnitudes of $T_{\max} = \max(T_x, T_y)$ and $T_{\min} = \min(T_x, T_y)$, respectively. The inclined lines within each ellipse give the orientation of maximum mechanical strength, with the weak direction perpendicular; the length of each line is $2\sqrt{T_x T_y}$. The statistics for model #34 are $T_x = 71 \pm 8 \text{ km}$, $T_y = 41 \pm 7 \text{ km}$, $\beta = 42 \pm 8^\circ$. Only two estimates (in the bottom-right) are $>20^\circ$ in error, and these points also exhibit the smallest anisotropy (i.e., $T_x \approx T_y$), so here β is inevitably poorly determined. We believe that such anomalies are a product of the random process used to generate the synthetic fractal models.

We have examined the six coherence plots at each point for some of the data sets. Although practically all of them show a very clear and quite smooth transition from high to low coherence, as in Fig. 4, many of them also show quite separate, but large, “spikes” or “humps” in coherence at higher wavenumbers in some azimuths. These also occur with real data: similar features can be seen in the 2D coherence plots in Fig. 11 of Simons et al. (2003). Because of the $1/|\mathbf{k}|$ weighting, mentioned in Section 4, these features usually have little effect on our inversions. Without the weighting, it is possible for an-

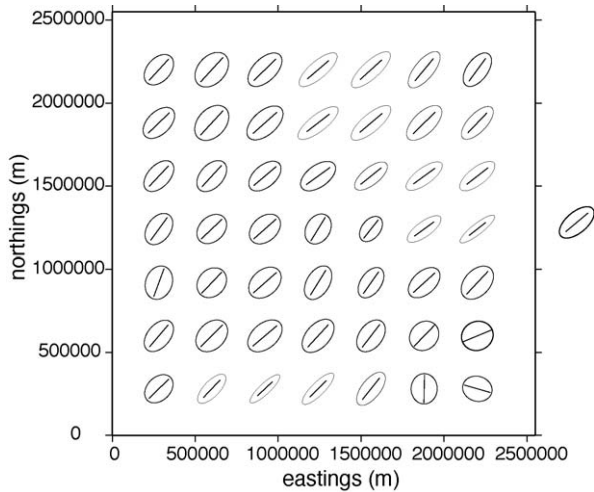


Fig. 5. Anisotropic elastic thickness ellipses from inversion of data for a Forsyth-style synthetic plate model (#34) with $T_x = 80$ km, $T_y = 40$ km and $\beta = 40^\circ$, with $f = 1$. The relative lengths of the semi-major and semi-minor ellipse axes indicate the degree of anisotropy in elastic thickness, while the orientation of the major axis (shown by the inclined lines of length $2\sqrt{T_x T_y}$ at the ellipse centres) indicates the direction of maximum mechanical strength. A model ellipse is shown to the right for comparison.

version to find a model which fits a long-wavelength transition at one azimuth together with a short-wavelength transition at another azimuth, resulting in a model with too large an anisotropy.

To compare the wavelet method against the Slepian multitaper ($K = NW = 3$) anisotropy estimates in Swain and Kirby (2003b), we also tested 100 pairs for a model with parameters $[100, 50, 0^\circ]$, using the global wavelet coherence. The wavelet method returned estimates of: $\bar{T}_x = 87 \pm 14$ km, $\bar{T}_y = 55 \pm 8$ km, and $\bar{\beta} = 2 \pm 12^\circ$; compared with $T_x = 68 \pm 11$ km, $T_y = 43 \pm 7$ km, and $\beta = -1 \pm 17^\circ$ from the multitaper method. The wavelet method gives a much better agreement with the model input parameters, particularly for the T_x estimate.

Finally, a further plate model was used to test the method, this time for a weaker plate, with parameters $[10, 30, 80^\circ]$. The estimates from the inversions of the 100 anisotropic wavelet coherences were: $\bar{T}_x = 14 \pm 2$ km, $\bar{T}_y = 26 \pm 3$ km, and $\bar{\beta} = 80 \pm 4^\circ$. Like the Fourier-based methods, it seems that the wavelet method better estimates smaller, rather than larger, values of elastic thickness.

The choice of initial estimates of $[T_x, T_y, \beta]$ in the inversion was not found to influence the final estimates of these parameters. Furthermore, computations on the 100 gravity/topography pairs using a smaller value of $\delta\theta$

(10°) in order to increase directional sampling, produced exactly the same results. Also, increasing the number of wavelet scales (from 28 to 56) had a negligible effect upon the outcome, and merely gave smoother coherence profiles. Finally, choosing a smaller value for $\Delta\theta$ of 45° gave a marginal increase in the variance of the parameter estimates of the uniform models. Hence, we believe that our sampling density in both azimuth- and scale-domains is adequate.

6. Application to Australian data

6.1. Australian gravity and topography data

Computations involving the Fourier transform on continental scales have to account for Earth curvature. To avoid errors arising from the planar treatment of curvilinear coordinates, all data were projected onto a Mercator grid, with origin at $133^\circ\text{E}, 0^\circ\text{N}$. This projection is conformal, thereby preserving angles, and is cylindrical, facilitating an intuitive visual interpretation of directions with respect to geographic parallels. In geographic coordinates, the study area spans approximately $101\text{--}165^\circ\text{E}$, and $2\text{--}49^\circ\text{S}$.

For the study area, grids of the topography/bathymetry and complete Bouguer anomaly were derived from the following data sets. The Australian land topography grid was derived from the GEODATA 9-arcsecond DEM (digital elevation model) of Australia (Geoscience Australia, 2001). The bathymetric data were taken from the GEBCO Digital Atlas, given at 1-arcminute spacing (National Oceanic and Atmospheric Administration, 2003), which are compiled from ship-track data only, and, importantly, not from inverted altimetry gravity (e.g., Smith and Sandwell, 1997). Topography over Indonesia and Papua New Guinea were also taken from the GEBCO Digital Atlas. Topography and bathymetry data were merged, and regridded at 20 km spacing on the Mercator grid.

Simple Bouguer anomalies over mainland Australia were taken from the 2004 release of Geoscience Australia's land gravity data base. Gravimetric terrain corrections derived from the 9-arcsecond DEM (Kirby and Featherstone, 1999) were added to these anomalies to form complete Bouguer anomalies over the continent. Over Indonesia and Papua New Guinea, free-air anomalies were derived from the EGM96 geopotential model to degree and order 360: simple Bouguer anomalies were computed from these using the above GEBCO topography data. Over marine areas we used free-air anomalies from the KMS02 satellite altimetry model (Andersen and Knudsen, 1998) at a 2-arcminute grid spacing. A ma-

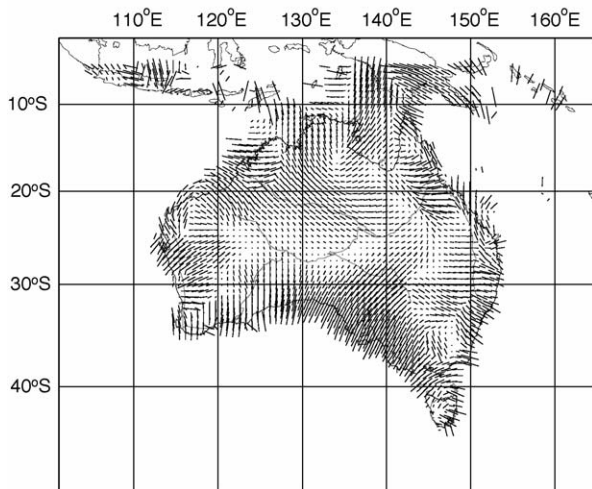


Fig. 6. Mechanical anisotropy in Australia: axes in the direction of T_{\min} and of length proportional to the anisotropy $(T_{\max} - T_{\min})/T_{\max}$. Also shown are the crustal mega-elements of Shaw et al. (1995). Mercator projection.

rine Bouguer anomaly was derived from these by applying a complete Bouguer correction computed from the GEBCO bathymetric model using the formula of Parker (1972). Again, the land and marine gravity data were merged and regridded at 20 km spacing on the Mercator grid.

6.2. Results and discussion

The bathymetry was first converted into a load by calculating the equivalent depth of the sea bottom if the salt water were replaced by air, i.e., multiplying the ocean water depth by $(\rho_c - \rho_w)/\rho_c$, where we used values of $\rho_c = 2800 \text{ kg m}^{-3}$ and $\rho_w = 1030 \text{ kg m}^{-3}$. Then, as for the synthetic models, the wavelet coherences were inverted, assuming $f = 1$, yielding T_x , T_y and β estimates at each grid node. For these data, however, we spatially averaged the auto- and cross-spectra into bins of size $80 \text{ km} \times 80 \text{ km}$. As discussed in Section 5, the bin size does not significantly alter the magnitudes of T_x , T_y , or β , and anisotropy maps generated using $160 \text{ km} \times 160 \text{ km}$ bins showed the same pattern of directions.

Fig. 6 shows the results plotted as bars, or ‘axes’, in the weak direction with length proportional to the anisotropy, here defined as $(T_{\max} - T_{\min})/T_{\max}$. We only show results for the landmasses and their continental shelves. Results over the deeper ocean are very scattered, probably due to the poor sampling of the bathymetry data over these areas. Occasionally the inversion does not converge to a solution, but this appears to be confined to offshore areas.

Fig. 6 clearly shows distinct clusters within Australia, containing homogeneous anisotropy directions. Sometimes the boundary between adjacent clusters exhibits a smooth, gradual change in direction, in other cases this change is abrupt. In addition, as previously noted by Simons et al. (2003), there is a clear tendency towards orthogonality between the axes shown in Fig. 6 and the Australian coastline.

Fig. 6 also shows the major boundaries of the Australian crustal mega-element map of Shaw et al. (1995). Although the correlation between these boundaries and the distribution of our weak axes is far from being general or precise, there are some good examples: one is the characteristic pattern over the Pilbara Craton (117°E , 23°S), mimicking its large scale structure. In other cases, such as the Kimberley (126°E , 16°S), North Australian (130°E , 18°S), and Gawler Cratons (135°E , 32°S), the anisotropy has a uniform, or slowly varying direction which changes more abruptly over their boundaries.

It is noticeable in Fig. 6 that the axes change direction more rapidly close to the coast than over the centre of Australia. This can be explained through the result of Swain and Kirby (2006) that T_e decreases in magnitude towards the Australian coastline, and through the fact that only mid- to small-scale wavelets are important when resolving the lower transition wavelengths associated with low T_e . Such wavelets have a smaller spatial extent, and can thus resolve more rapid changes in both T_e and anisotropy direction.

7. Correlations with other data

It is not an aim of this paper to give a detailed review of the possible geophysical controls on T_e and its anisotropy, which has been provided elsewhere (e.g., Lowry and Smith, 1995; Simons et al., 2000, 2003), other than to note that their methods can all be approximated by our intrinsically anisotropic plate model (Swain and Kirby, 2003b). Nevertheless, in order to give the reader the opportunity to judge the truth of the anisotropy axes shown in Fig. 6, we will give a comparison with some other relevant data over Australia, namely: (a) previous studies of isostatic anisotropy; (b) the stress map; (c) seismic azimuthal anisotropy.

7.1. Previous isostatic studies

The previous studies of Australian isostatic anisotropy have all used fixed windows of varying size from $720 \text{ km} \times 720 \text{ km}$ (Simons et al., 2003) to $2200 \text{ km} \times 2200 \text{ km}$ (Swain and Kirby, 2003b), implying averaging over areas encompassing many of

the axes in Fig. 6 and making comparisons difficult. The closest comparable result to ours is Fig. 12b of Simons et al. (2003), which shows axes of implied weakness derived from the maximum transition wavelength of the coherence. Their window width is small enough to downward bias estimates of both T_e and transition wavelength in Australia by more than a factor of three (Swain and Kirby, 2003a). This bias would affect estimates of the *amplitude* of anisotropy (which Simons et al. (2003) did not make), but not of its direction. However the bias may well compromise the accuracy of the orientations.

Fig. 7 shows a comparison of the “long-wavelength weak directions” from Fig. 12b of Simons et al. (2003) with the axes shown in Fig. 6 calculated by averaging the wavelet spectra over their window size (720 km \times 720 km). This figure shows their “good” quality (thick, white bars) and “fair” quality (thick, grey bars) measurements, but omits both “bad” and “null” results (Simons et al., 2003). However, we have included our axes at the locations of their missing measurements, and a majority of these (7/12) show relatively small anisotropy. The agreement between their “good” measurements and ours in Fig. 7 is excellent: 9 out of 15 are within 30° , which has a $<2.2\%$ chance of being random. For all 28 of the Simons et al. (2003) measurements (i.e., “good” and “fair”), 14 of ours agree to within 30° , implying a 2.9% chance of random occurrence. Overall, we think that the agreement between the two studies is encouraging.

7.2. Tectonic stress

Lowry and Smith (1995) state that azimuthal variations of T_e reflect tectonic stress, because such stress reduces T_e in the direction of the stress axis. Their study is of the western US Cordillera, a region of extensional stress, and in several of their tectonic provinces they observe excellent agreement between the minor axes of T_e ellipses (i.e., the weak directions) and directions of minimum horizontal compressive stress (i.e., the direction of tectonic stress). They note, however, some exceptions to this (e.g., Yellowstone).

The Australian stress regime is largely compressive (Zoback, 1989) so the correlation should be between the T_e minor axis and the direction of maximum horizontal compressive stress. The Australian stress map, unlike those of most other continents, shows orientations of maximum horizontal compressive stress that are variable and not generally parallel to the direction of absolute plate motion (north to north–northeast) (e.g., Hillis and Reynolds, 2003). Because of the variable stress ori-

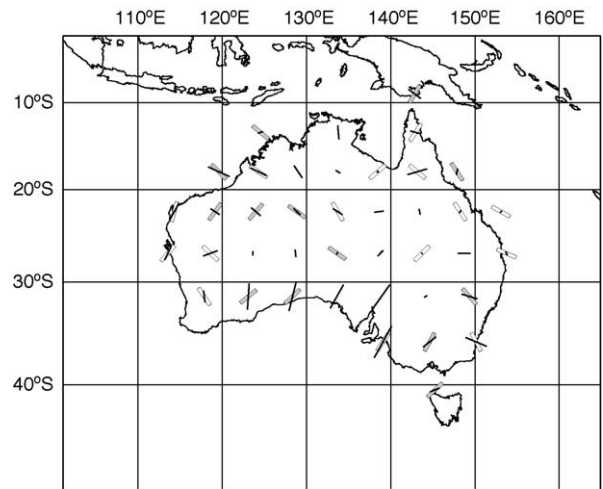


Fig. 7. Comparison of our axes of anisotropy in the direction of T_{\min} (averaged over a 720 km \times 720 km area) (thin, black bars), with the Simons et al. (2003) “long-wavelength weak directions” (“good” data: thick, white bars; “fair” data: thick, grey bars). Our axes are also shown where Simons et al. (2003) record “null” or “bad” data. Mercator projection.

entations, Hillis and Reynolds (2003) define a number of “stress provinces” for each of which they calculate a mean stress orientation. The data are very sparse and occur in concentrations, mostly within sedimentary basins since the majority of them are from measurements in petroleum exploration boreholes. Thus the mean stress orientations are heavily weighted towards the uppermost crust. Eleven of the twelve Australian stress provinces defined by Hillis and Reynolds (2003) show statistically significant stress orientations, of which nine are from offshore or coastal basins, and two from interior basins (the Cooper and Amadeus Basins).

Fig. 8 compares the stress province data with the weak directions in our Fig. 6, averaged over 400 km \times 400 km windows. There is little correlation between the two sets of directions. In two cases our weak directions may be too scattered for a useful comparison, and four cases are offshore basins, where, as we have previously noted, the T_e results are less reliable. Overall, however, it appears that tectonic stress is not a major control on the lithospheric strength anisotropy that we observe. This agrees with the conclusions of Simons et al. (2003), who contend that there would only be a relation between the two if present-day stress and fossil strain are still related. However, another factor may be the stress magnitudes: although the observed stress data do not include magnitudes, model stresses are typically less than 30 MPa (Reynolds et al., 2003; Zhao and Müller, 2003). Reference to Fig. 4b of Lowry and Smith (1995) shows that

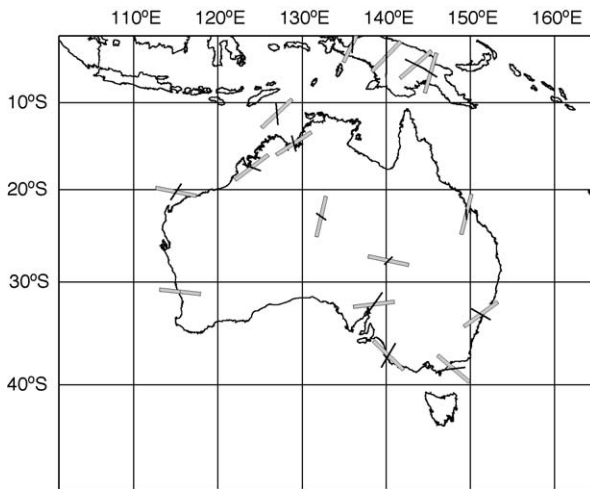


Fig. 8. Comparison of our axes of anisotropy in the direction of T_{\min} (averaged over a $400 \text{ km} \times 400 \text{ km}$ area) (thin, black bars), with the mean stress orientations in the Australian stress provinces of Hillis and Reynolds (2003) (thick, grey bars). Mercator projection.

such stress magnitudes would probably have no significant effect on T_c .

7.3. Seismic anisotropy

Seismic anisotropy under the continents is usually studied using shear wave splitting of near-vertical core phases like SKS (Silver, 1996). For Australia such studies have tended to measure mostly weak or null splitting (Debayle and Kennett, 2003). This is most likely because of the inherent lack of vertical resolution of the method, usually requiring the assumption of a single anisotropic layer, which is probably an oversimplification for Australia. Although it is sometimes possible to interpret shear wave splitting data in terms of two anisotropic layers, this requires fairly numerous data with a range of backazimuths, which have not been available for most Australian studies. An exception is the detailed study by Girardin and Farra (1998) of data from the Canberra GEOSCOPE station.

Recently, some tomographic models derived from surface waves have included azimuthal anisotropy. Although there is a trade-off between heterogeneity and anisotropy (e.g., Simons et al., 2002), tests show that including anisotropy clearly fits the data better and it has the advantage of significant depth resolution. Tomographic studies of Australian seismic anisotropy include Simons et al. (2002) and Debayle and Kennett (2003) who both present maps of SV-wave azimuthal anisotropy from inversion of Rayleigh waveform data. However, both of these studies were hampered by a sparsity of ray

paths for Western Australia. Kennett et al. (2004) show a more recent model which includes many more ray paths under Western Australia.

Although these models of seismic anisotropy are rather different in detail, there is general agreement (e.g., Debayle and Kennett, 2003; Simons et al., 2003) that the seismic azimuthal anisotropy observed under Australia at depths of $<150\text{--}200 \text{ km}$ is quite variable, with as many E–W as N–S orientations, while at depths $>200 \text{ km}$ the orientations are consistently N–S to NNE–SSW. Simons et al. (2003) examined the orthogonality between the directions of shallower seismic anisotropy and those of mechanical anisotropy, concluding that they represent “frozen” deformation from the most recent episode of orogeny. There is general agreement that the anisotropy at depths $>200 \text{ km}$ reflects present-day deformation due to the northward motion of the Australian Plate. Silver (1996) refers to the “frozen” deformation mechanism as ‘vertically coherent deformation’ (VCD), and to the deformation due to plate motion as ‘simple asthenospheric flow’ (SAF), explaining them in terms of preferential alignment of olivine crystals in response to finite strain.

Simons et al. (2003) suggest that over most of Precambrian Australia, where compressional tectonics predominate, the weak directions from isostatic analyses should lie approximately at right angles to the fast axes in the shallower mantle layers of the seismic models, because for VCD the fast axes should be approximately perpendicular to the compression direction, which is also the direction that has accumulated the most deformation per unit of topographic loading. They compared the weak directions for their “good” measurements, to the fast axes of their seismic model (Simons et al., 2002), finding that they are approximately at right angles in $>50\%$ of cases at the shallowest depth of their model (30 km), falling to 30% at 200 km depth. However, the fact that this comparison was based on only 15 measurements of the long-wavelength coherence anisotropy somewhat reduced the impact of this study.

We have obtained a recent update of the anisotropic model of Kennett et al. (2004) for 3 depths: 75, 125 and 175 km (S. Fishwick, personal communication, 2005). The model consists of azimuth and amplitude (%) of the anisotropy, and shear velocity given on a $3^\circ \times 3^\circ$ grid. In Figs. 9–11 we compare the seismic anisotropy with our weak direction axes, the latter calculated by averaging the spectra over a window size of $300 \text{ km} \times 300 \text{ km}$. The length scale for the seismic anisotropy axes is 1/30 of that of the isostatic weak axes. At all three depths there is a strong tendency for the axes to lie at a large angle to one another, particularly for inland Australia west of about 143°E . At 75 km, but not at the other depths, there seems

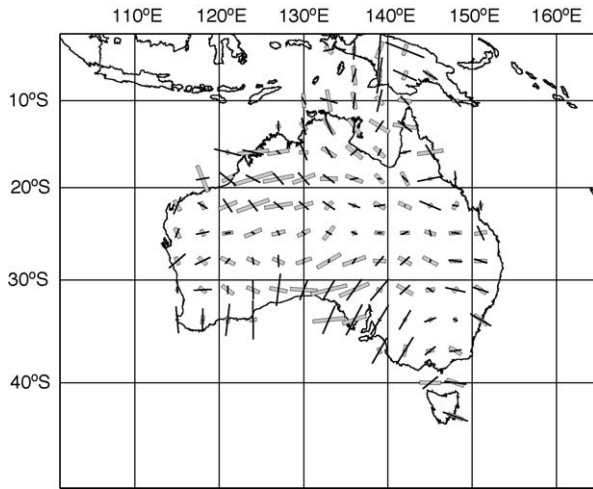


Fig. 9. Comparison of our axes of anisotropy in the direction of T_{\min} (averaged over a $300 \text{ km} \times 300 \text{ km}$ area) (thin, black bars), with the fast axes of seismic anisotropy from the tomographic model of Kennett et al. (2004) at 75 km depth (thick, grey bars). Mercator projection.

to be a relation between the amplitudes of anisotropy of the two data sets: their orthogonality appears to improve with depth. In eastern Australia there is less correlation apparent between the two sets of axes, but this might be expected since the seismic tomography of Kennett et al. (2004) shows that the lithosphere is much thinner here, so the depths 125–175 km probably represent asthenosphere.

We have carried out tests with circular statistics on a subset of 57 pairs of axes from Figs. 9–11 within an area west of 143°E and between latitudes 33°S and 14°S , approximately corresponding to the extent of Precambrian basement. We first applied a Rayleigh test to

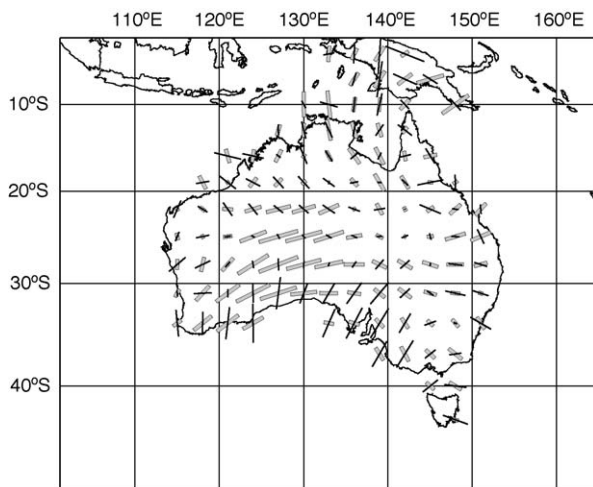


Fig. 10. As Fig. 9, but at 125 km depth.

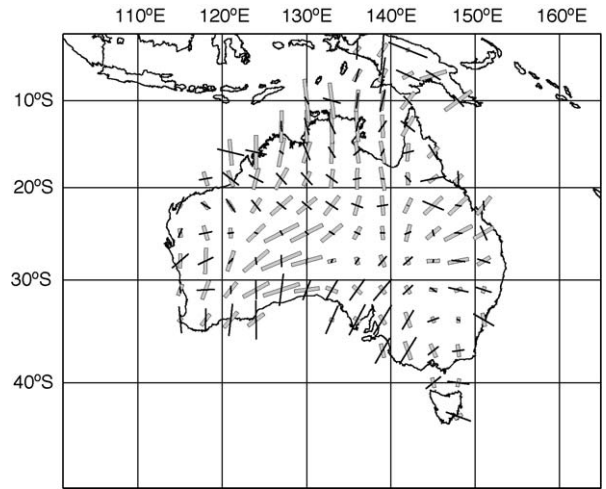


Fig. 11. As Fig. 9, but at 175 km depth.

the hypothesis that differences in orientation between the mechanically weak axes and the fast seismic axes are sampled from a uniform distribution, with no preferred direction, versus the alternative hypothesis that they are from a von Mises distribution - the circular equivalent of a normal distribution (Davis, 1986). Next we tested the hypothesis that the differences have a mean of 90° . Since the data are orientations, they were doubled prior to the calculations, and the angular results subsequently halved (Davis, 1986). The results are given as, for the first test, mean resultant vectors (\bar{R}) and significance levels (α), and for the second test, mean orientations (A) and 95% confidence intervals. They are as follows: for 75 km, $\bar{R} = 0.238$, $\alpha = 4\%$, $A = 101 \pm 25^\circ$; for 125 km, $\bar{R} = 0.278$, $\alpha = 1\%$, $A = 87 \pm 21^\circ$; for 175 km, $\bar{R} = 0.477$, $\alpha = < 1\%$, $A = 86 \pm 11^\circ$. Thus, for all three depths, we can say, with $>96\%$ confidence, that the orientation differences have a preferred direction and that the 95% confidence intervals around all three mean orientations include 90° .

8. Conclusions

We have described a technique for mapping the mechanical anisotropy of the elastic lithosphere which yields greater detail than previously possible. The method gave good results with a wide variety of synthetic, anisotropic, uniform models. Applied to new grids of Australian topography and gravity data it gave a map of minimum T_e directions which is in reasonable agreement with the “long-wavelength weak directions” of Simons et al. (2003). Although both studies suffer from various uncertainties which would contribute to differences between the results, we think that the use in the

latter study of a fixed window of width comparable to, or even smaller than, the transition wavelength over much of Precambrian Australia, probably results in relatively large estimation errors.

We have compared our results with a recent model of seismic azimuthal anisotropy (Kennett et al., 2004) at depths between 75 and 175 km. Over Precambrian Australia, results of a statistical analysis carried out on the differences in orientation between our weak axes and the fast seismic axes strongly support the hypothesis that they are orthogonal. We are therefore in agreement with Simons et al. (2003) that the source of our observed anisotropy is likely to be vertically coherent “frozen” deformation of the lithosphere (Silver, 1996) due to alignment of olivine crystals. The fact that our results correlate with seismic azimuthal anisotropy at depths of 75–175 km also supports the ideas that under cratonic regions crust and mantle are strongly coupled and that the strength of the lithosphere resides mainly in the upper mantle (Vauchez et al., 1998).

Comparison of our weak axes with a map of present day stress directions (Hillis and Reynolds, 2003) shows that there is no obvious plate weakening in these directions, probably because the stresses are too small.

We have also indicated how our wavelet approach can be modified so that the predicted coherences are modelled without the assumption of a constant loading ratio (Forsyth’s method). A comparison between the two methods will be the subject of a further paper, but we note that our results to date indicate that using Forsyth’s method will not change any of the above conclusions.

Acknowledgements

The authors thank Frederik Simons, Scott Reynolds, Richard Hillis, Stewart Fishwick and Brian Kennett for their anisotropy data, Geoscience Australia for the supply of terrestrial gravity and topography data, and Ole B. Andersen and Per Knudsen for the altimetry gravity grid. We also thank the three anonymous reviewers, whose helpful comments greatly improved this contribution.

Appendix A. Theoretical coherence from the Banks and Forsyth plate models

A.1. Theoretical coherence from the Banks model

The theoretical coherence for an anisotropic Banks et al. (2001)-style plate with plate constants [T_x , T_y , β], and a wavenumber-dependent subsurface to surface loading ratio, $f(\mathbf{k})$, is given by [cf. Eqs. (14), (11) and (12) in

Banks et al. (2001)]:

$$\gamma_t^2(\mathbf{k}) = 1 - \frac{(\alpha_T/\beta_T - \alpha_B/\beta_B)^2}{(1 + 1/A^2)(\alpha_T/\beta_T)^2 + (1 + A^2)(\alpha_B/\beta_B)^2}, \quad (\text{A.1})$$

where A , α_T , α_B , β_T , and β_B are all functions of wavenumber, \mathbf{k} :

$$A(\mathbf{k}) = -f(\mathbf{k}) \frac{\rho_c g}{\Lambda(\mathbf{k}) + \Delta\rho g}, \quad (\text{A.2})$$

and

$$\alpha_T(\mathbf{k}) = \frac{-2\pi G \Delta\rho e^{-|\mathbf{k}|z_m}}{\Lambda(\mathbf{k}) + \rho_m g},$$

$$\alpha_B(\mathbf{k}) = \alpha_T(\mathbf{k}) + \frac{2\pi G e^{-|\mathbf{k}|z_1}}{g}, \quad (\text{A.3})$$

$$\beta_T(\mathbf{k}) = \beta_B(\mathbf{k}) + \frac{1}{\rho_c g}, \quad \beta_B(\mathbf{k}) = \frac{-1}{\Lambda(\mathbf{k}) + \rho_m g}, \quad (\text{A.4})$$

$\Lambda(\mathbf{k})$ is given by Eqs. (18) or (26). Note that Banks’s Eq. (19) are incorrect, and the above Eqs. (A.3) and (A.4) are the corrected versions of these, updated for anisotropy. In the isotropic case $D_x = D_y = D$, $\mathbf{k} \rightarrow |\mathbf{k}|$, and $\Lambda(\mathbf{k}) \rightarrow D|\mathbf{k}|^4$, as noted in Section 3.1.

As mentioned in Section 4, in this study we have assumed $f(\mathbf{k}) = 1$, $\forall \mathbf{k}$.

A.2. Theoretical coherence from the Forsyth model

If Forsyth (1985)’s Eqs. (4), (7) and (12) are substituted into his Eq. (25), the following analytical expression for a theoretical coherence can be derived, updated to account for anisotropy:

$$\gamma_t^2(\mathbf{k}) = \frac{[\xi + \phi f^2 r^2]^2}{[\xi^2 + f^2 r^2][1 + \phi^2 f^2 r^2]}, \quad (\text{A.5})$$

where ξ and ϕ are functions of \mathbf{k} (as is f) and are given in our Eq. (22), and $r = \rho_c/\Delta\rho$. Note that if the layer of variable density in the Banks model is placed at the Moho (i.e., $z_1 = z_m$), the Banks and Forsyth theoretical coherences are identical.

References

- Addison, P.S., 2002. The Illustrated Wavelet Transform Handbook. Institute of Physics Publishing.
- Andersen, O.B., Knudsen, P., 1998. Global marine gravity field from the ERS-1 and Geosat geodetic mission altimetry. *J. Geophys. Res.* 103 (C4), 8129–8137.

- Antoine, J.-P., Murensi, R., Vanderghaynst, P., Ali, S.T., 2004. Two-dimensional Wavelets and their Relatives. Cambridge University Press.
- Artemieva, I.M., Mooney, W.D., 2001. Thermal thickness and evolution of Precambrian lithosphere: a global study. *J. Geophys. Res.* 106 (B8), 16387–16414.
- Audet, P., Mareschal, J.-C., 2004. Anisotropy of the flexural response of the lithosphere in the Canadian Shield. *Geophys. Res. Lett.* 31 (20), L20601 (doi:10.1029/2004GL021080).
- Banks, R.J., Parker, R.L., Huestis, S.P., 1977. Isostatic compensation on a continental scale: local versus regional mechanisms. *Geophys. J. R. Astron. Soc.* 51, 431–452.
- Banks, R.J., Francis, S.C., Hipkin, R.G., 2001. Effects of loads in the upper crust on estimates of the elastic thickness of the lithosphere. *Geophys. J. Int.* 145, 291–299.
- Burov, E.B., Diament, M., 1995. The effective elastic thickness (T_e) of continental lithosphere: what does it really mean? *J. Geophys. Res.* 100 (B3), 3905–3927.
- Chevrot, S., van der Hilst, R.D., 2000. The Poisson ratio of the Australian crust: geological and geophysical implications. *Earth Planet. Sci. Lett.* 183, 121–132.
- Comer, R.P., 1983. Thick plate flexure. *Geophys. J. R. Astron. Soc.* 72, 101–113.
- Davis, J.C., 1986. *Statistics and Data Analysis in Geology*, 2nd ed. Wiley, New York.
- Debayle, E., Kennett, B.L.N., 2003. Surface-wave studies of the Australian region. In: Hillis, R.R., Müller, R.D. (Eds.), *Evolution and Dynamics of the Australian Plate*. *Geol. Soc. Austr. Special Paper* 22, and *Geol. Soc. Am. Special Paper* 372, pp. 25–40.
- Farge, M., 1992. Wavelet transforms and their applications to turbulence. *Annu. Rev. Fluid Mech.* 24, 395–457.
- Forsyth, D.W., 1985. Subsurface loading and estimates of the flexural rigidity of continental lithosphere. *J. Geophys. Res.* 90 (B14), 12623–12632.
- Geoscience Australia, 2001. GEODATA 9 Second DEM Version 2. http://www.ga.gov.au/nmd/products/digidat/dem_9s.htm.
- Girardin, N., Farra, V., 1998. Azimuthal anisotropy in the upper mantle from observations of P-to-S converted phases: application to southeast Australia. *Geophys. J. Int.* 133, 615–629.
- Grossman, A., Morlet, J., 1984. Decomposition of Hardy functions into square integrable wavelets of constant shape. *SIAM J. Math. Anal.* 15 (4), 723–736.
- Hillis, R.R., Reynolds, S.D., 2003. In situ stress field of Australia. In: Hillis, R.R., Müller, R.D. (Eds.), *Evolution and Dynamics of the Australian Plate*. *Geol. Soc. Austr. Special Paper* 22, and *Geol. Soc. Am. Special Paper* 372, pp. 49–58.
- Kennett, B.L.N., Fishwick, S., Heintz, M., 2004. Lithospheric structure in the Australian region—a synthesis of surface wave and body wave studies. *Expl. Geophys.* 35 (4), 242–250.
- Kirby, J.F., 2005. Which wavelet best reproduces the Fourier power spectrum? *Comp. Geosci.* 31 (7), 846–864.
- Kirby, J.F., Featherstone, W.E., 1999. Terrain correcting Australian gravity observations using the national digital elevation model and the fast Fourier transform. *Aust. J. Earth Sci.* 46 (4), 555–562.
- Kirby, J.F., Swain, C.J., 2004. Global and local isostatic coherence from the wavelet transform. *Geophys. Res. Lett.* 31 (24), L24608 (doi:10.1029/2004GL021569).
- Lowry, A.R., Smith, R.B., 1994. Flexural rigidity of the Basin and Range–Colorado Plateau–Rocky Mountain transition from coherence analysis of gravity and topography. *J. Geophys. Res.* 99 (B10), 20123–20140.
- Lowry, A.R., Smith, R.B., 1995. Strength and rheology of the western U.S. Cordillera. *J. Geophys. Res.* 100 (B9), 17947–17963.
- Macario, A., Malinverno, A., Haxby, W.F., 1995. On the robustness of elastic thickness estimates obtained using the coherence method. *J. Geophys. Res.* 100 (B8), 15163–15172.
- McNutt, M.K., 1990. Flexure reveals great depth. *Nature* 343 (6259), 596–597.
- National Oceanic and Atmospheric Administration, 2003. General Bathymetric Chart of the Oceans. <http://www.ngdc.noaa.gov/mgg/gebco/grid/development.pdf>.
- Parker, R.L., 1972. The rapid calculation of potential anomalies. *Geophys. J. R. Astron. Soc.* 31, 447–455.
- Peitgen, H.-O., Saupe, D., 1988. *The Science of Fractal Images*. Springer.
- Pérez-Gussinyé, M., Lowry, A.R., Watts, A.B., Velicogna, I., 2004. On the recovery of effective elastic thickness using spectral methods: examples from synthetic data and from the Fennoscandian Shield. *J. Geophys. Res.* 109 (B10), B10409 (doi:10.1029/2003JB002788).
- Poudjom Djomani, Y.H., Fairhead, J.D., Griffin, W.L., 1999. The flexural rigidity of Fennoscandia: reflection of the tectonothermal age of the lithospheric mantle. *Earth Planet. Sci. Lett.* 174, 139–154.
- Reynolds, S.D., Coblentz, D.D., Hillis, R.R., 2003. Influences of plate-boundary forces on the regional intraplate stress field of continental Australia. In: Hillis, R.R., Müller, R.D. (Eds.), *Evolution and Dynamics of the Australian Plate*. *Geol. Soc. Austr. Special Paper* 22, and *Geol. Soc. Am. Special Paper* 372, pp. 59–70.
- Shaw, R.D., Wellman, P., Gunn, P., Whitaker, A.J., Tarlowski, C., Morse, M., 1995. Australian crustal elements map. *AGSO Res. Newslett.* 23, 1–3.
- Silver, P.G., 1996. Seismic anisotropy beneath the continents: probing the depths of geology. *Annu. Rev. Earth Planet. Sci.* 24, 385–432.
- Simons, F.J., Zuber, M.T., 2000. Isostatic response of the Australian lithosphere: estimation of effective elastic thickness and anisotropy using multitaper spectral analysis. *J. Geophys. Res.* 105 (B8), 19163–19184.
- Simons, F.J., van der Hilst, R.D., Montagner, J.-P., Zielhuis, A., 2002. Multimode Rayleigh wave inversion for heterogeneity and azimuthal anisotropy of the Australian upper mantle. *Geophys. J. Int.* 151, 738–754.
- Simons, F.J., van der Hilst, R.D., Zuber, M.T., 2003. Spatiospectral localization of isostatic coherence anisotropy in Australia and its relation to seismic anisotropy: implications for lithospheric deformation. *J. Geophys. Res.* 108 (B5), 2250 (doi:10.1029/2001JB000704).
- Smith, W.H.F., Sandwell, D.T., 1997. Global seafloor topography from satellite altimetry and ship depth soundings. *Science* 277, 1957–1962.
- Stark, C.P., Stewart, J., Ebinger, C.J., 2003. Wavelet transform mapping of effective elastic thickness and plate loading: validation using synthetic data and application to the study of southern African tectonics. *J. Geophys. Res.* 108 (B12), 2558 (doi:10.1029/2001JB000609).
- Swain, C.J., Kirby, J.F., 2003a. The effect of ‘noise’ on estimates of the elastic thickness of the continental lithosphere by the coherence method. *Geophys. Res. Lett.* 30 (11), 1574 (doi:10.1029/2003GL017070).
- Swain, C.J., Kirby, J.F., 2003b. The coherence method using a thin anisotropic elastic plate model. *Geophys. Res. Lett.* 30 (19), 2014 (doi:10.1029/2003GL018350).
- Swain, C.J., Kirby, J.F., 2006. An effective elastic thickness map of Australia from wavelet transforms of gravity and topogra-

- phy using Forsyth's method. *Geophys. Res. Lett.* 33 (2), L02314 (doi:10.1029/2005GL025090).
- Timoshenko, S.P., Woinowsky-Krieger, S., 1959. *Theory of Plates and Shells*. McGraw-Hill.
- Vaucher, A., Tommasi, A., Barruol, G., 1998. Rheological heterogeneity, mechanical anisotropy and deformation of the continental lithosphere. *Tectonophysics* 296, 61–86.
- Watts, A.B., 1978. An analysis of isostasy in the world's oceans. 1. Hawaiian-Emperor seamount chain. *J. Geophys. Res.* 83 (B12), 5989–6004.
- Watts, A.B., 2001. *Isostasy and Flexure of the Lithosphere*. Cambridge University Press.
- Watts, A.B., Burov, E.B., 2003. Lithospheric strength and its relationship to the elastic and seismogenic layer thickness. *Earth Planet. Sci. Lett.* 213, 113–131.
- Wolf, D., 1985. Thick plate flexure re-examined. *Geophys. J. R. Astron. Soc.* 80, 265–273.
- Zhao, S., Müller, R.D., 2003. Three-dimensional finite-element modelling of the tectonic stress field in continental Australia. In: Hillis, R.R., Müller, R.D. (Eds.), *Evolution and Dynamics of the Australian Plate*. *Geol. Soc. Austr. Special Paper* 22, and *Geol. Soc. Am. Special Paper* 372, pp. 71–89.
- Zoback, M.L., and 28 others, 1989. Global patterns of tectonic stress. *Nature* 341, 291–298.